Investigation of Large Scale Traveling Atmospheric/Ionospheric Disturbances using the Coupled SAMI3 and GITM Models

A. Bukowski[1], A. Ridley[2], J. D. Huba[3] , C. Valladares[1], and P. C. Anderson[1]

[1] The University of Texas at Dallas, W. B. Hanson Center for Space Sciences, Richardson, Texas, USA.

[2] The University of Michigan, Ann Arbor, USA

[3] Syntek Technologies, Fairfax, VA, USA

Corresponding authorAaron Bukowski (aaron.bukowski@utdallas.edu)

Key Points:

- We demonstrate that traveling ionospheric disturbances can be produced in simulations of the ionosphere-thermosphere system.
- We show that these traveling ionospheric disturbances propagate to the topside ionosphere in simulations.

Abstract

We present simulation results of the vertical structure of Large Scale Traveling Ionospheric Disturbances (LSTIDs) during synthetic geomagnetic storms. These data are produced using a one-way coupled SAMI3/GITM model, where GITM (Global Ionosphere Thermosphere Model) provides thermospheric information to SAMI3 (SAMI3 is Another Model of the Ionosphere), allowing the production and propagation of LSTIDs. We show simulation results which demonstrate that the traveling atmospheric disturbances (TADs) generated in GITM propagate to the topside ionosphere in SAMI3 as LSTIDs. The speed and wavelength (900 m/s and 10º-20º latitude) are consistent with LSTID observations in storms of similar magnitudes. We demonstrate the LSTIDs reach altitudes beyond the topside ionosphere with amplitudes of <5% over background which will facilitate the use of plasma measurements from the topside ionosphere to supplement measurements from GNSS in the study of TIDs. Additionally, we demonstrate the dependence of the characteristics of these TADs and TIDs on longitude.

Plain Language Summary

LSTIDs are a type of wave that occurs in the ionosphere, a layer of the atmosphere dominated by plasma where the motions of particles are highly subject to the magnetic field, during geomagnetic storms. We utilize two models of Earth's atmosphere and ionosphere to show how these waves behave and show that their location, timing, and speed is dependent on various storm characteristics, timing, and location. We also show that a high-altitude satellite measuring plasma density in the ionosphere should be able to detect the characteristics of these waves.

1 Introduction

During geomagnetic storms, Traveling Atmospheric Disturbances (TADs), are generated by locally heating the thermosphere within the auroral zone and propagating the deposited energy outwards. The energy is deposited primarily through Joule heating caused by precipitating particles colliding with neutrals, which results in frictional heating and momentum exchange with ions and electrons (Brekke & Kamide, 1996; Hunsucker, 1982; Strangeway, 2012; J. Zhu et al., 2016). TADs propagate as variations in density, temperature, and winds in the neutral atmosphere. These neutral wind perturbations drive their ionospheric counterpart, Traveling Ionospheric Disturbances (TIDs), through ion-drag forcing. TADs/TIDs can also be driven from below by volcanos, thunderstorms, thermospheric turbulence, etc. which form atmospheric gravity waves (AGWs) in the lower thermosphere (Borchevkina et al., 2021; Cheng & Huang, 1992; Nicholls & Pielke, 2000; Pradipta et al., 2023; Zhang et al., 2022). Few observations exist of AGWs due to their location in the lower thermosphere, however TADs have been observed with satellites such as the Gravity field and steady-state Ocean Circulation Explorer (GOCE) and the Challenging Minisatellite Payload (CHAMP) (Trinh et al., 2018). Most of the studies of TIDs are performed with data from ground-based networks such as ionosondes (Hajkowicz, 1991), radars (Bowman, 1990; Fukao et al., 1991; Oliver et al., 1995), and airglow imagers (Shiokawa et al., 2004). Recently, Ground-based Global Navigation Satellite System (GNSS) networks have allowed investigations on a more global scale (Figueiredo et al., 2018; Pradipta et al., 2016). However, such measurements are altitude integrated and cannot decipher the wave characteristics at different altitudes. Ionospheric measurements from satellites can provide information on TIDs where GNSS receivers cannot be placed, but such measurements typically do not correlate well with GNSS perturbation TEC

measurements where they do coincide (Ren et al., 2022). Thus, it is important to understand the characteristics of the altitude dependence of TIDs.

Large Scale TIDs (LSTIDs) are TIDs with wavelengths greater than ~1000 km and are normally associated with geomagnetic storms, although they have been observed at geomagnetically quiet times with smaller amplitudes (Bruinsma & Forbes, 2010; Hedin & Mayr, 1987). The electron and ion density perturbations associated with LSTIDs are mainly observed with ground-based radars and GNSS receivers (Pradipta et al., 2016; van de Kamp et al., 2014; Zakharenkova et al., 2016), with the clear disadvantage that these observations can only be acquired over land and in areas with sufficient power and communication infrastructure. The ionosphere is a medium whose refractive index is dependent on the integrated electron density along the path of the radio wave. GNSS receivers measure the delay associated with the integrated electron density along the line-of-sight to the GNSS satellites which is processed into integrated Total Electron Content (TEC) and subsequently geometrically converted to vertical TEC. TEC measurements yield little insight into the vertical structure of LSTIDs and the lack of data over the oceans prevents a global view of LSTID propagation during geomagnetic storms. While work is being done to form a more complete global picture of LSTID propagation using low power GNSS receivers and amateur radio networks, these are not yet widespread and still lack coverage over the oceans.

Satellite observations of LSTIDs have been performed, but the link between measurements made at different altitudes in the ionosphere and the vertically integrated TEC is unclear (Ren et al., 2022). Analysis of Dynamic Explorer (DE 2) data yielded observations of wavelike fluctuations, only in the high-latitude regions (Innis & Conde, 2002). The Global Ultraviolet Imager (GUVI) instrument onboard the Thermosphere Ionosphere Mesosphere Energetics and Dynamics (TIMED) satellite has recently been used to identify GWs/LSTIDs/LSTADs and link them to observations by ground-based interferometers and radars; however, these observations do not extend into the topside ionosphere (Bossert et al., 2022). Sounding from satellites above the F-peak is possible and Gross (1985) compared topside sounding observations to in-situ ionization density measurements suggesting that perturbations follow flux tubes vertically, but was not able to prove if the perturbations seen were travelling or stationary.

The use of global circulation ionosphere and thermosphere models is therefore necessary to link observations between measurements made in different layers of the atmosphere and to understand the behavior of LSTIDs both vertically and longitudinally. The thermosphere–ionosphere–electrodynamics general circulation model (TIE-GCM) has been used to model LSTADs/LSTIDs (Jonah et al., 2020; Richmond, 2003; Roble & Ridley, 1994). However TIE-GCM does not model altitudes above ~500-700 km (depending on solar activity), well short of satellites with capabilities to measure properties of the topside ionosphere (720 km and 840 km for COSMIC-2 and DMSP, respectively). The Whole Atmosphere Community Climate Model with thermosphere and ionosphere extension (WACCM-X) has been used to model LSTIDs as well (Liu et al., 2018), but reaches altitudes similar to that of TIE-GCM.

Investigations using SAMI3 (SAMI is another model of the ionosphere) have demonstrated that it can sustain high-altitude TIDs using the HIgh Altitude Mechanistic general Circulation Model (HIAMCM) (Huba et al., 2023) and WACCM-X (Huba & Liu, 2020) for the neutral dynamics to simulate GWs generated in the lower atmosphere. In this study, we use the Global Ionosphere-Thermosphere Model (GITM), which can self consistently generate TADs, as

a seeding mechanism for SAMI3. When coupled, we can use the results from SAMI3 to investigate how LSTIDs, seeded by LSTADs, behave in the ionosphere up to topside and exospheric altitudes.

2 Methodology

2.1 GITM

GITM is a global-scale 3-dimensional model with an adjustable, radially-aligned orthogonal geographic, grid. GITM solves the coupled continuity, momentum, and energy equations for the neutral and ion species in a user-specified grid stretched in altitude. GITM differs from most thermospheric models in that it does not assume hydrostatic equilibrium in the vertical velocity solver, which allows the realistic generation of TADs due to Joule and particle heating in the auroral zone. GITM allows different models of high-latitude electric fields, auroral particle precipitation, solar EUV, and particle energy deposition to be used (Ridley et al., 2006). The work presented here uses the Weimer (2005) model, driven by solar wind inputs for the high-latitude electric potential, and Fuller-Rowell and Evans (1987) model, driven by the Hemispheric Power Index (HPI) for the auroral particle heating, which drives TAD production. The initial state of the model is set by the Mass Spectrometer and Incoherent Scatter radar (MSIS) neutral atmosphere model and the International Reference Ionosphere (IRI) model.

2.2 SAMI3

SAMI3 is a 3-dimensional, physics-based model of the ionosphere. SAMI3 also solves the coupled continuity, momentum, and energy equations, however it only models ions and electrons (not neutral species). By default, SAMI3 uses NRLMSISE00 (Picone et al., 2002) for neutral densities and the HWM14 (Drob et al., 2015) for the neutral wind; it has been modified to use GITM neutral densities and winds to allow more accurate representations of neutral dynamics and generation of TADs. SAMI3 also uses Weimer for high-latitude electric potential.

SAMI3 is configured to read the density of the neutral species N2, O2, O, NO, N4S, H, and He, as well as the zonal and meridional neutral winds and neutral temperature from GITM every five minutes. This data is interpolated from the geographic grid used by GITM to the geomagnetic grid used by SAMI3 with magnetic Apex coordinates (Richmond, 1995; VanZandt et al., 1972). Because SAMI3 extends above the GITM domain, the neutral velocities and temperatures in this region are assumed to be constant, while the densities are assumed to decrease hydrostatically. SAMI3 is set to output data at a five-minute cadence as well.

2.3 Synthetic Geomagnetic Storm

We use a synthetic geomagnetic storm to investigate our ability to produce LSTIDs using the coupled GITM/SAMI3 model and examine their characteristics in altitude, local time, and longitude. We have chosen a day with very low background geomagnetic activity (May 21, 2011) and run the models with the quiet-time indices and seasonally appropriate conditions associated with this time. Representing a moderate to large geomagnetic storm, we increase the background values of Bz=-2 nT and HPI=10 GW to Bz=-20 nT and HPI=200 GW as a step function. All other geomagnetic indices were kept at constant values. Both models were run for at least 24 hours before the onset of the simulated storm to eliminate transients and reach steady state.

3 Results and Discussion

Figures 1 a–f show the TADs produced in the simulation using GITM. The perturbations were calculated by first removing background densities with a first-order forward-backward bandpass filter with cutoff frequencies at 40 and 85 minutes, and then calculating the percent difference between the model outputs and filtered data. TADs form immediately after storm onset and propagating towards the equator. These perturbations form in, and propagate away from, the auroral zone where most of the energy from Joule heating and particle precipitation is deposited. While not shown, similar propagation is observed in all neutral densities as well as the neutral winds.

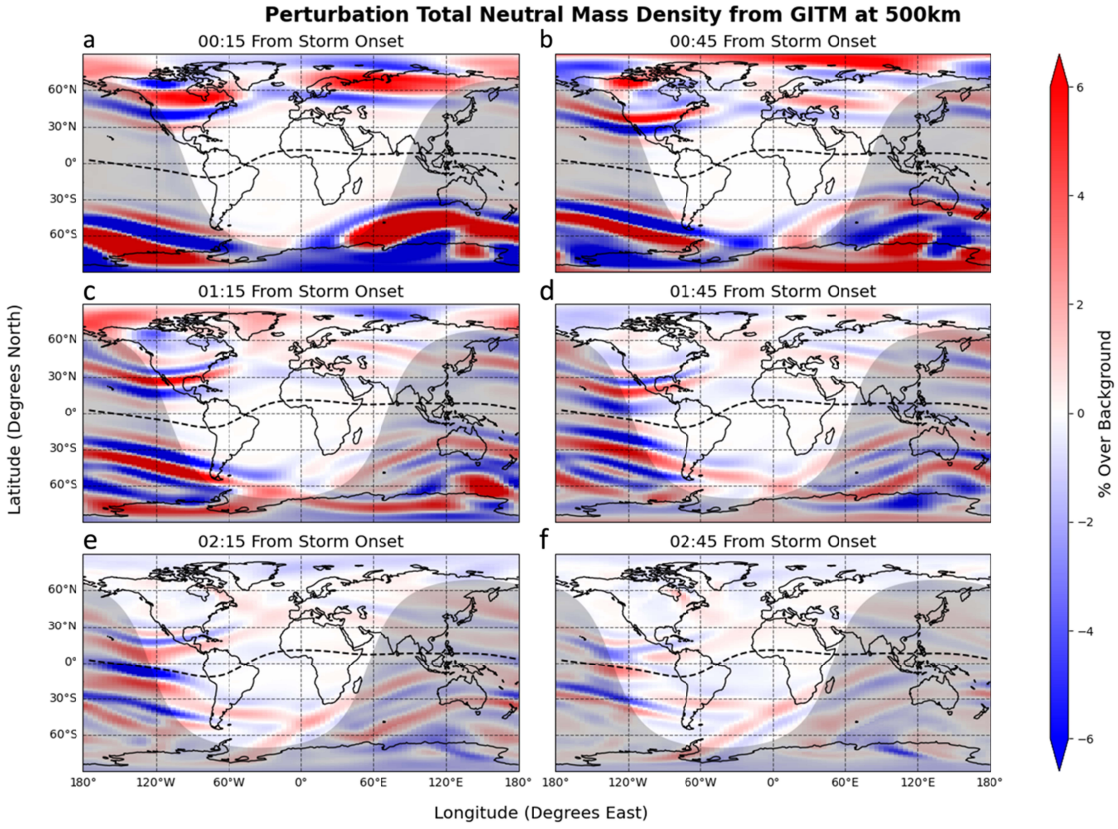

Figure 1. Global snapshots of perturbation total neutral density output from GITM as a function of time from storm onset. The location of the magnetic equator is indicated with the black dashed line.

The speed of these TADs (~900 m/s) is consistent with LSTIDs measured with detrended TEC data from GNSS observations in geomagnetic storms of similar amplitude in Bz and HPI. Bz often oscillates throughout the duration of a geomagnetic storm, signaling changes in amount of energy deposited into the Ionosphere-Thermosphere (IT) system. These variations in deposited energy cause variations in the neutral winds and temperatures in the auroral zone, producing TADs that propagate equatorward. Our model only has one change in drivers (Bz and HPI), leading to a singular TAD being produced.

Figures 2 a–d show keograms of the perturbations in the total neutral mass density at various longitudes starting 3 hours before storm onset and extending to 8 hours after storm onset. Due to the filtering technique used (with the filter centered at each time and the abrupt change in

density not having a single frequency the bandpass filter can react to), perturbations from background appear before storm onset, though this is not physical as only a single perturbation was formed. The LSTAD propagates equatorward with some asymmetries in amplitude and speed with longitude and hemisphere. The hemispherical asymmetries are due the temperature being lower in the winter (Southern) hemisphere. Longitudinal asymmetries are due to the local time/geographic distribution of the locations of the heating in the auroral zone (see Figure 4).

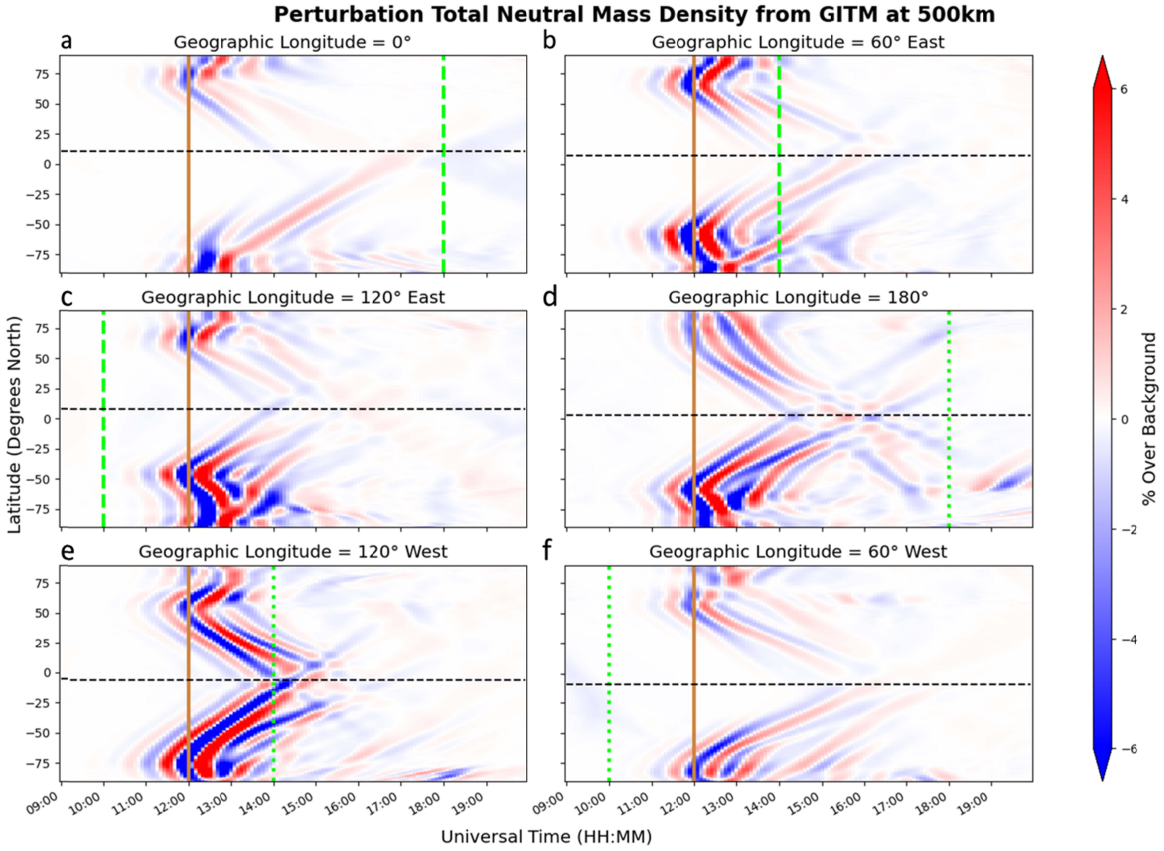

Figure 2. Keograms of Total Neutral Density at 500 km altitude and several geographic longitudes. Solid brown vertical lines at 12 UT mark storm onset. Dashed vertical green lines mark local dusk while dotted vertical green lines mark local dawn. At each longitude, the location of the magnetic equator is indicated with the horizontal black dashed line.

At lower altitudes the propagation speed and amplitude of TADs are smaller than at higher altitudes which is due to decreased temperatures, seen in Figures 3a-f. There appears to be two distinct modes, rather than a gradual transition, which could be evidence of different propagation modes in the thermosphere or, as proposed by Hedin & Mayr (1987), a ducted propagation mode. At 150 km (Figures 3a-c), perturbations reach the equator between 15-16 UT while at 660 km (Figures 3d-f), the perturbations reach the equator near 13-14 UT. The keograms show that the TADs propagate both poleward and equatorward from the auroral zone. The perturbations that appear delayed, between 2 and 3 hours after storm onset, are from TADs that propagated from their auroral source region across the polar cap.

There is a strong longitudinal dependence of the TAD distribution. This is largely due to the distribution of energy input in the auroral zone being a function of local time. Figure 4 shows the locations of the greatest intensities of Joule heating in the auroral zone, and thus the regions

where TADs are produced. Because these locations are dependent on magnetic local time (MLT), and in turn UT/longitude, the longitudinal distribution of TADs will be dependent on the UT of their production (Perlongo & Ridley, 2016).

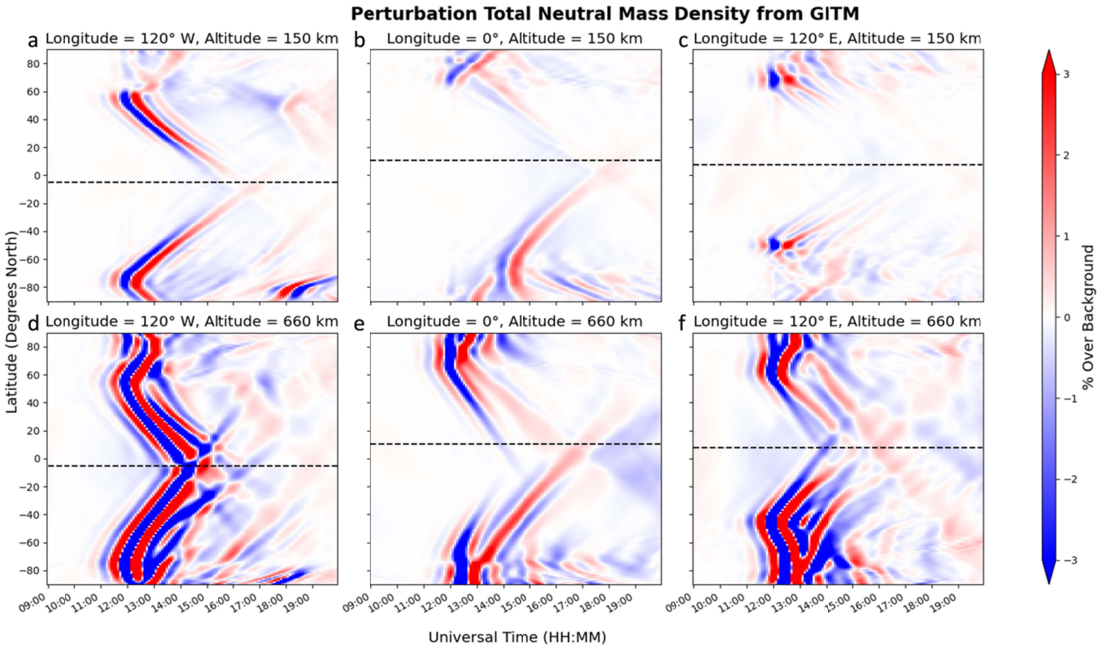

Figure 3. Keograms of perturbation total neutral density from GITM along ±120° & 0° geographic longitude and at 150 km (top panels) and 660 km (bottom panels) altitude. The location of the magnetic equator is indicated with the black dashed line.

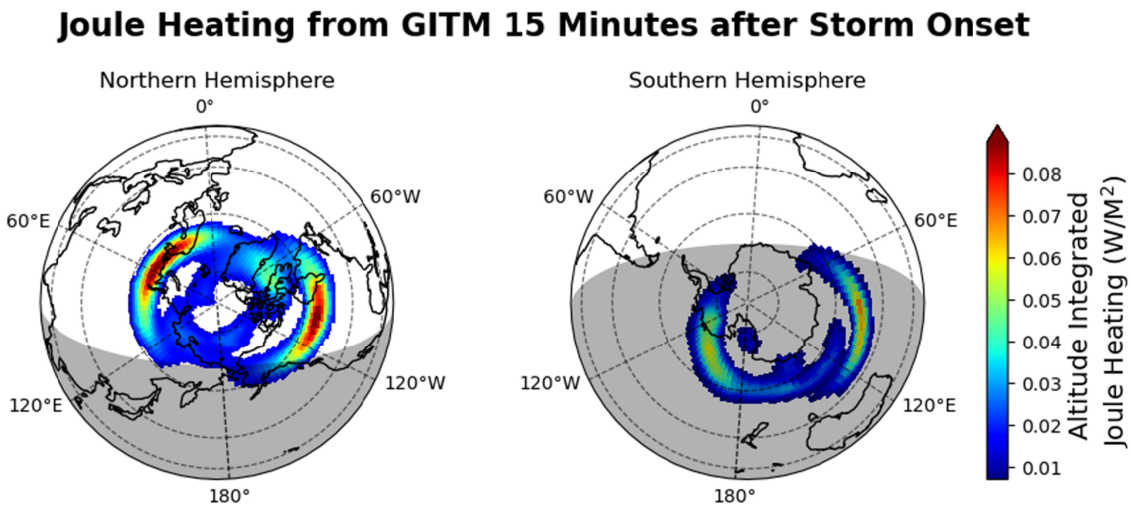

Figure 4. Altitude integrated Joule heating just after storm onset. Correlation between the locations with the greatest amplitude of Joule heating and the locations where TADs are formed in Figures 1-3 is evident

The greatest heating in the northern hemisphere occurs in the 60° E and 100°W geographic longitude (GLON) sectors and are offset from the geographic pole by about 20°

geographic latitude (GLAT). In the southern hemisphere, the peak heating occurs near 75° and 65° S GLAT, and 90° E and 140° W GLON. The greater offset between the geographic and geomagnetic field is evident at these geographic locations. This offset thus leads to longitudinal and hemispherical asymmetries, as the location of the auroral zone is dependent on Earth's magnetic field configuration and the timing of storm onset (Perlongo & Ridley, 2016).

Motion of the modeled TADs is associated with the neutral winds (and the LSTAD dynamics), which then drive ion motion through momentum exchange. The ionospheric counterpart of the TADs we have produced with GITM are shown in Figures 5a-f, which show keograms at the same longitudes as those shown in Figure 2. The perturbations are extracted from SAMI3 outputs with the same methods used for the GITM outputs. The speed and wavelength of these TIDs (900 m/s and ~10-20o latitude, respectively) would classify them as Large Scale. LSTIDs for a storm of this magnitude have been observed to have an amplitude between 0.7-1.5 TEC Units (TECU) with GNSS receivers. Our slightly smaller amplitude is consistent with previously reported results showing that existing particle precipitation models do not account for the full spectrum of precipitating electrons, leading to lower auroral energy inputs (Q. Zhu et al., 2022).

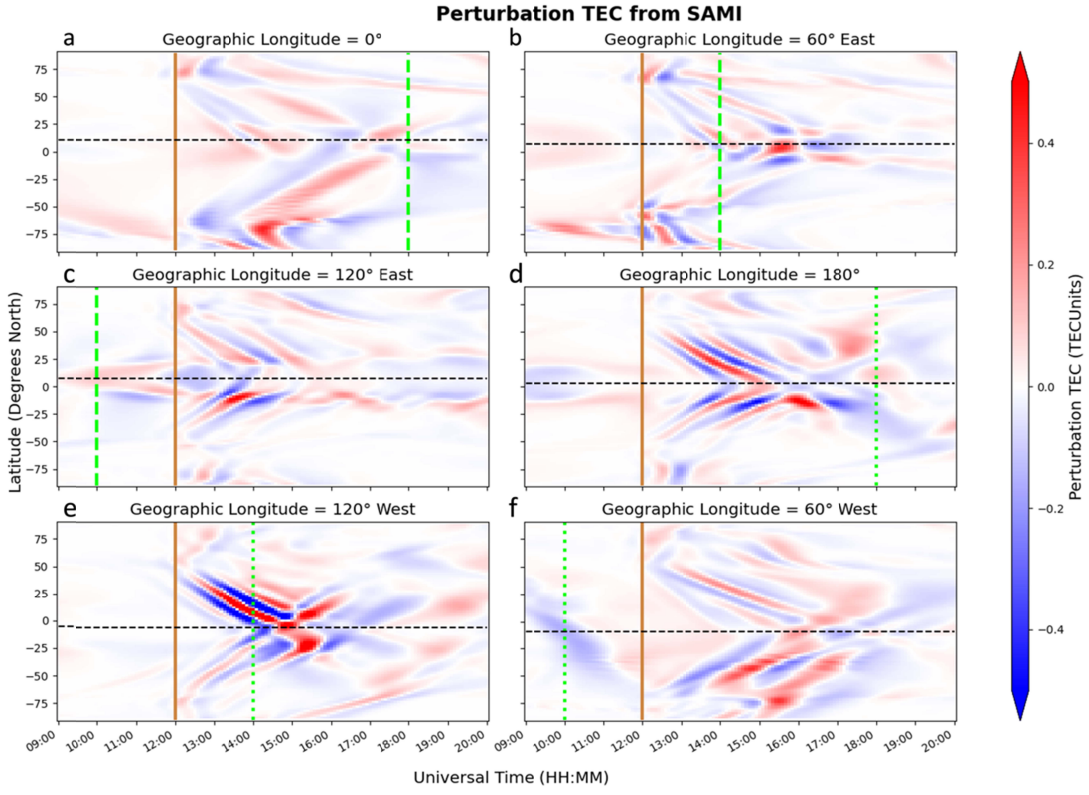

Figure 5. Keograms of SAMI3 differential TEC along several geographic longitudes. As in Figure 2, the solid line marks storm onset, dashed vertical green lines mark local dusk, and dotted vertical green lines mark local dawn. The location of the magnetic equator at each longitude is indicated with the horizontal black dashed line.

The LSTIDs originate in the auroral zone in both hemispheres, propagate to the equator and continue into the opposite hemisphere. At the longitudes in Figures 5a, 5b and 5f, the TIDs meet North of the geomagnetic equator due to the background temperature being higher in the

summer hemisphere. On the nightside this effect is less pronounced (as interhemispheric temperature differences are lower in the nightside), with the LSTIDs meeting very close to the geomagnetic equator in Figures 5c-e. Hemispheric asymmetries in LSTID amplitude and wavelength also exist, where the longitudes with the greatest hemispheric symmetry correspond to the longitudes with the most similar Joule heating rates in the North and South hemisphere, near 0° and 180° longitude (Figures 5a and 5d). In general, the discrepancy in amplitude and propagation speed between the two hemispheres is due to the storm occurring during Northern summer and thus the greater deposition of energy in the Northern auroral zone, as seen in Figure 4.

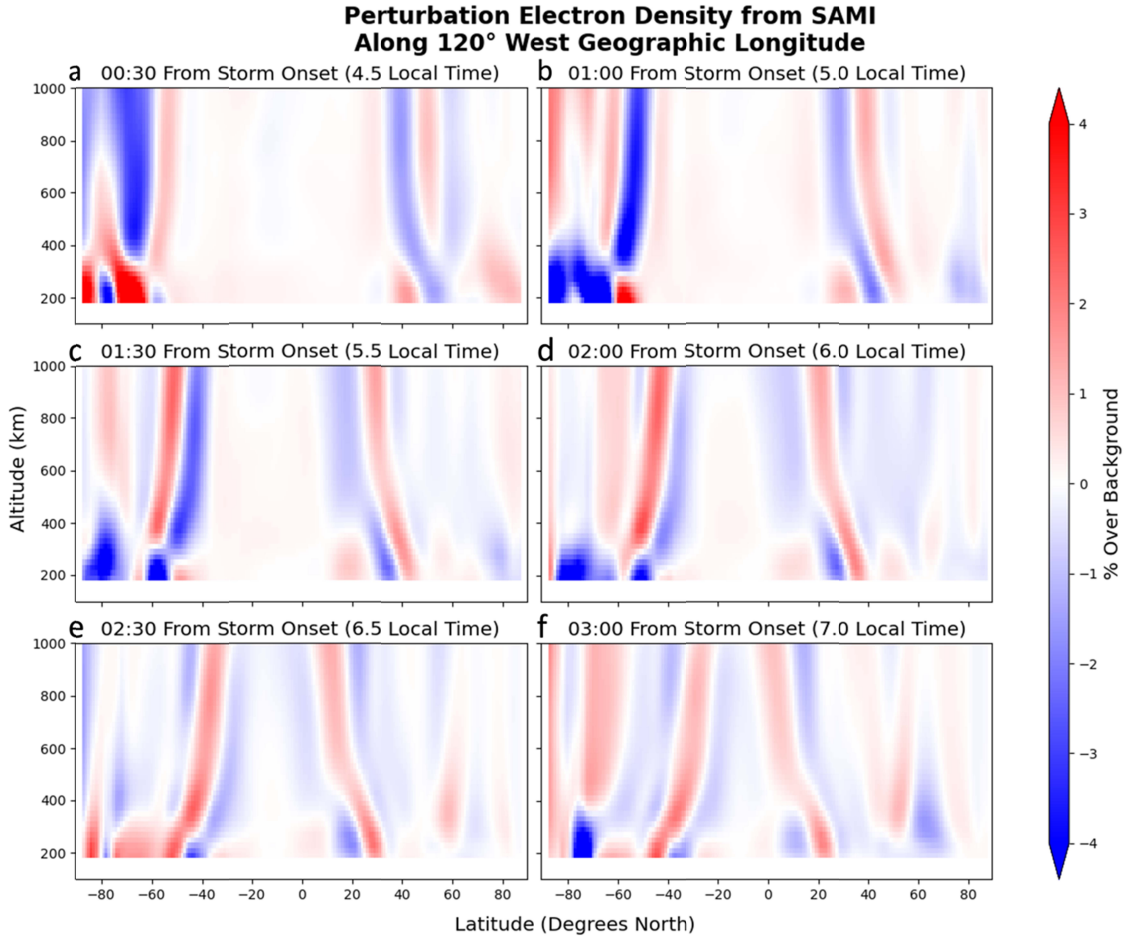

Figure 6. Propagation of TIDs shown with perturbation electron density along a single geographic longitude modeled in SAMI3. The magnetic equator at this longitude is at approximately -5° Geographic latitude.

Figure 6 shows the altitudinal distribution of LSTIDs produced in SAMI3 along a single geographic longitude. Other longitudes show similar behavior. Perturbations in electron density exist throughout the entire ionosphere and well into the topside. A reversal in perturbation density can be seen at around 300-400 km, where the F-peak lies. The electron density variation depends on the sign of $V \cdot \nabla N_e$ and since the sign of ∇N_e changes above the F-peak, the sign of the perturbation changes (Huba et al., 2015). This reversal is a contributing factor to why the perturbations in vertically integrated TEC perturbations are of a lower amplitude than the

perturbations seen in the electron density and why satellite measurements in the topside ionosphere typically do not correlate well with GNSS perturbation TEC measurements.

4 Conclusions

Through a one-way coupled GITM and SAMI3 model, we have utilized a synthetic geomagnetic storm to investigate TAD and LSTID behavior. We have shown that, due to the location of their formation in the auroral zone, there is a longitudinal dependence of TAD/LSTID location associated with the location of maximum Joule heating. TADs/LSTIDs can be seen forming immediately after storm onset and propagating both equatorward and poleward with speeds and amplitudes that vary with altitude. The most intense LSTID and TAD occurred at 120° W longitude. This region does not correspond to the most intense Joule heating, but near sunrise when the neutral temperatures are the lowest, and thus where the perturbations over background are largest. LSTIDs produced in the SAMI3 results show speeds that are consistent with detrended TEC data from GNSS observations in geomagnetic storms of similar amplitude in Bz and HPI. They propagate equatorward, however the locations where LSTIDs produced in each hemisphere meet with respect to the geographic equator vary with longitude due the offset of the geomagnetic and geographic equators. The LSTIDs are seen to extend well into the topside ionosphere; however, the sign of the associated density perturbations reverses near the F-peak, explaining why satellite measurements in the topside ionosphere typically do not correlate well with GNSS perturbation TEC measurements.

The simulated storm can be further utilized to model LSTIDs during different seasons and with different storm onset times, allowing us to determine the role of the offset between the geographic and geomagnetic poles on LSTID characteristics. Our results aid our understanding of the longitudinal, altitudinal, and hemispherical behavior/distribution of LSTIDs as well as various aspects of IT coupling during geomagnetic storms. Using the modeled results in the topside ionosphere, we will be able to deconvolve the differences between TEC and satellite measurements and utilize observations from satellites, such as DMSP, to fill gaps in TEC observations in areas where GNSS receivers cannot be placed.

Acknowledgments

The work by Aaron Bukowski was supported by NASA grant 80NSSC20K0195. The work by Phillip Anderson was supported by NASA grants 80NSSC22K017 and 80NSSC20K0195. The work of J.D. Huba was supported by NASA grant 80NSSC20K0190 We would like to acknowledge high-performance computing support from Cheyenne (Computational And Information Systems Laboratory, 2017), sponsored by the National Science Foundation.

Open Research

The GITM model is open source and can be accessed at https://github.com/gitmcode/gitm. The SAMI3 model is available at https://doi.org/10.5281/zenodo.7895859. Data used to recreate the plots shown in this publication can be accessed at (Bukowski, 2023). An analysis suite for processing of both model outputs is available at https://github.com/abukowski21/SAMI3-GITM-python/.

References

Borchevkina, O. P., Adamson, S. O., Dyakov, Y. A., Karpov, I. V., Golubkov, G. V., Wang, P.-K., & Golubkov, M. G. (2021). The Influence of Tropospheric Processes on Disturbances in the D and E Ionospheric Layers. *Atmosphere*, *12*(9), 1116. https://doi.org/10.3390/atmos12091116

Bossert, K., Paxton, L. J., Matsuo, T., Goncharenko, L., Kumari, K., & Conde, M. (2022). Large-Scale Traveling Atmospheric and Ionospheric Disturbances Observed in GUVI With Multi-Instrument Validations. *Geophysical Research Letters*, *49*(16). https://doi.org/10.1029/2022GL099901

Bowman, G. G. (1990). A review of some recent work on mid-latitude spread-F occurrence as detected by ionosondes. *Journal of Geomagnetism and Geoelectricity*, *42*(2), 109–138. https://doi.org/10.5636/jgg.42.109

Brekke, A., & Kamide, Y. (1996). On the relationship between Joule and frictional heating in the polar ionosphere. *Journal of Atmospheric and Terrestrial Physics*, *58*(1–4), 139–143. https://doi.org/10.1016/0021-9169(95)00025-9

Bruinsma, S. L., & Forbes, J. M. (2010). Anomalous behavior of the thermosphere during solar minimum observed by CHAMP and GRACE. *Journal of Geophysical Research: Space Physics*, *115*(A11). https://doi.org/10.1029/2010JA015605

Bukowski, A. (2023). *Data From SAMI3/GITM Simulations of a Synthetic Geomagnetic Storm*. https://doi.org/10.5281/ZENODO.8264079

Cheng, K., & Huang, Y.-N. (1992). Ionospheric disturbances observed during the period of Mount Pinatubo eruptions in June 1991. *Journal of Geophysical Research*, *97*(A11), 16995. https://doi.org/10.1029/92JA01462

311 Computational And Information Systems Laboratory. (2017). *Cheyenne: SGI ICE XA Cluster*.
312 https://doi.org/10.5065/D6RX99HX
313 Drob, D. P., Emmert, J. T., Meriwether, J. W., Makela, J. J., Doornbos, E., Conde, M.,
314 Hernandez, G., Noto, J., Zawdie, K. A., McDonald, S. E., Huba, J. D., & Klenzing, J. H.
315 (2015). An update to the Horizontal Wind Model (HWM): The quiet time thermosphere.
316 *Earth and Space Science*, *2*(7), 301–319. https://doi.org/10.1002/2014EA000089
317 Figueiredo, C. A. O. B., Takahashi, H., Wrasse, C. M., Otsuka, Y., Shiokawa, K., & Barros, D.
318 (2018). Medium-Scale Traveling Ionospheric Disturbances Observed by Detrended Total
319 Electron Content Maps Over Brazil. *Journal of Geophysical Research: Space Physics*.
320 https://doi.org/10.1002/2017JA025021
321 Fukao, S., Kelley, M. C., Shirakawa, T., Takami, T., Yamamoto, M., Tsuda, T., & Kato, S.
322 (1991). Turbulent upwelling of the mid-latitude ionosphere: 1. Observational results by
323 the MU radar. *Journal of Geophysical Research*, *96*(A3), 3725.
324 https://doi.org/10.1029/90JA02253
325 Fuller-Rowell, T. J., & Evans, D. S. (1987). Height-integrated Pedersen and Hall conductivity
326 patterns inferred from the TIROS-NOAA satellite data. *Journal of Geophysical Research*,
327 *92*(A7), 7606. https://doi.org/10.1029/JA092iA07p07606
328 Gross, S. H. (1985). Large scale structures from topside sounding. *Radio Science*, *20*(3), 499–
329 510. https://doi.org/10.1029/RS020i003p00499
330 Hajkowicz, L. A. (1991). Global onset and propagation of large-scale travelling ionospheric
331 disturbances as a result of the great storm of 13 March 1989. *Planetary and Space*
332 *Science*, *39*(4), 583–593. https://doi.org/10.1016/0032-0633(91)90053-D

Hedin, A. E., & Mayr, H. G. (1987). Characteristics of wavelike fluctuations in Dynamics Explorer neutral composition data. *Journal of Geophysical Research*, *92*(A10), 11159. https://doi.org/10.1029/JA092iA10p11159

Huba, J. D., Becker, E., & Vadas, S. L. (2023). Simulation Study of the 15 January 2022 Tonga Event: Development of Super Equatorial Plasma Bubbles. *Geophysical Research Letters*, *50*(1), e2022GL101185. https://doi.org/10.1029/2022GL101185

Huba, J. D., Drob, D. P., Wu, T.-W., & Makela, J. J. (2015). Modeling the ionospheric impact of tsunami-driven gravity waves with SAMI3: Conjugate effects: TSUNAMI IONOSPHERE EFFECTS. *Geophysical Research Letters*, *42*(14), 5719–5726. https://doi.org/10.1002/2015GL064871

Huba, J. D., & Liu, H.-L. (2020). Global Modeling of Equatorial Spread F with SAMI3/WACCM-X. *Geophysical Research Letters*, *47*(14), e2020GL088258. https://doi.org/10.1029/2020GL088258

Hunsucker, R. D. (1982). Atmospheric gravity waves generated in the high-latitude ionosphere: A review. *Reviews of Geophysics*, *20*(2), 293–315. https://doi.org/10.1029/RG020i002p00293

Innis, J. L., & Conde, M. (2002). Characterization of acoustic-gravity waves in the upper thermosphere using Dynamics Explorer 2 Wind and Temperature Spectrometer (WATS) and Neutral Atmosphere Composition Spectrometer (NACS) data: POLAR CAP ACOUSTIC-GRAVITY WAVES. *Journal of Geophysical Research: Space Physics*, *107*(A12), SIA 1-1-SIA 1-22. https://doi.org/10.1029/2002JA009370

Jonah, O. F., Zhang, S., Coster, A. J., Goncharenko, L. P., Erickson, P. J., Rideout, W., de Paula, E. R., & de Jesus, R. (2020). Understanding Inter-Hemispheric Traveling Ionospheric

356 Disturbances and Their Mechanisms. *Remote Sensing*, *12*(2), 228.
357 https://doi.org/10.3390/rs12020228
358 Liu, H., Bardeen, C. G., Foster, B. T., Lauritzen, P., Liu, J., Lu, G., Marsh, D. R., Maute, A.,
359 McInerney, J. M., Pedatella, N. M., Qian, L., Richmond, A. D., Roble, R. G., Solomon,
360 S. C., Vitt, F. M., & Wang, W. (2018). Development and Validation of the Whole
361 Atmosphere Community Climate Model With Thermosphere and Ionosphere Extension
362 (WACCM-X 2.0). *Journal of Advances in Modeling Earth Systems*, *10*(2), 381–402.
363 https://doi.org/10.1002/2017MS001232
364 Nicholls, M. E., & Pielke, R. A., Sr. (2000). Thermally Induced Compression Waves and Gravity
365 Waves Generated by Convective Storms. *Journal of the Atmospheric Sciences*, *57*, 3251–
366 3271. https://doi.org/10.1175/1520-0469(2000)057<3251:TICWAG>2.0.CO;2
367 Oliver, W. L., Fukao, S., Sato, M., Otsuka, Y., Takami, T., & Tsuda, T. (1995). Middle and
368 upper atmosphere radar observations of the dispersion relation for ionospheric gravity
369 waves. *Journal of Geophysical Research*, *100*(A12), 23763.
370 https://doi.org/10.1029/95JA02520
371 Perlongo, N. J., & Ridley, A. J. (2016). Universal time effect in the response of the thermosphere
372 to electric field changes. *Journal of Geophysical Research: Space Physics*, *121*(4), 3681–
373 3698. https://doi.org/10.1002/2015JA021636
374 Picone, J. M., Hedin, A. E., Drob, D. P., & Aikin, A. C. (2002). NRLMSISE-00 empirical model
375 of the atmosphere: Statistical comparisons and scientific issues: TECHNIQUES. *Journal*
376 *of Geophysical Research: Space Physics*, *107*(A12), SIA 15-1-SIA 15-16.
377 https://doi.org/10.1029/2002JA009430

Pradipta, R., Carter, B. A., Currie, J. L., Choy, S., Wilkinson, P., Maher, P., & Marshall, R. (2023). On the Propagation of Traveling Ionospheric Disturbances From the Hunga Tonga-Hunga Ha'apai Volcano Eruption and Their Possible Connection With Tsunami Waves. *Geophysical Research Letters*, *50*(6), e2022GL101925. https://doi.org/10.1029/2022GL101925

Pradipta, R., Valladares, C. E., Carter, B. A., & Doherty, P. H. (2016). Interhemispheric propagation and interactions of auroral traveling ionospheric disturbances near the equator. *Journal of Geophysical Research: Space Physics*, *121*(3), 2462–2474. https://doi.org/10.1002/2015JA022043

Ren, X., Mei, D., Liu, H., & Zhang, X. (2022). Investigation on Horizontal and Vertical Traveling Ionospheric Disturbances Propagation in Global-Scale Using GNSS and Multi-LEO Satellites. *Space Weather*, *20*(5). https://doi.org/10.1029/2022SW003041

Richmond, A. D. (1995). Ionospheric Electrodynamics Using Magnetic Apex Coordinates. *Journal of Geomagnetism and Geoelectricity*, *47*(2), 191–212. https://doi.org/10.5636/jgg.47.191

Richmond, A. D. (2003). Long-lasting disturbances in the equatorial ionospheric electric field simulated with a coupled magnetosphere-ionosphere-thermosphere model. *Journal of Geophysical Research*, *108*(A3), 1118. https://doi.org/10.1029/2002JA009758

Ridley, A. J., Deng, Y., & Tóth, G. (2006). The global ionosphere–thermosphere model. *Journal of Atmospheric and Solar-Terrestrial Physics*, *68*(8), 839–864. https://doi.org/10.1016/j.jastp.2006.01.008

Roble, R. G., & Ridley, E. C. (1994). A thermosphere-ionosphere-mesosphere-electrodynamics general circulation model (time-GCM): Equinox solar cycle minimum simulations (30-

500 km). *Geophysical Research Letters*, *21*(6), 417–420. https://doi.org/10.1029/93GL03391

Shiokawa, K., Otsuka, Y., Ogawa, T., Saito, A., Ohshima, K., Kubota, M., Nakamura, T., Yamamoto, M., Maruyama, T., & Wilkinson, P. (2004). *Geomagnetic conjugate observation of medium-scale traveling ionospheric disturbances: FRONT3 campaign*.

Strangeway, R. J. (2012). The equivalence of Joule dissipation and frictional heating in the collisional ionosphere. *Journal of Geophysical Research: Space Physics*, *117*(A2), 2011JA017302. https://doi.org/10.1029/2011JA017302

Trinh, Q. T., Ern, M., Doornbos, E., Preusse, P., & Riese, M. (2018). Satellite observations of middle atmosphere–thermosphere vertical coupling by gravity waves. *Annales Geophysicae*, *36*(2), 425–444. https://doi.org/10.5194/angeo-36-425-2018

van de Kamp, M., Pokhotelov, D., & Kauristie, K. (2014). TID characterised using joint effort of incoherent scatter radar and GPS. *Annales Geophysicae*, *32*(12), 1511–1532. https://doi.org/10.5194/angeo-32-1511-2014

VanZandt, T. E., Clark, W. L., & Warnock, J. M. (1972). *Magnetic apex coordinates: A magnetic coordinate system for the ionospheric F2 layer* (noaa:32775). https://repository.library.noaa.gov/view/noaa/32775

Weimer, D. R. (2005). Improved ionospheric electrodynamic models and application to calculating Joule heating rates. *Journal of Geophysical Research*, *110*(A5), A05306. https://doi.org/10.1029/2004JA010884

Zakharenkova, I., Astafyeva, E., & Cherniak, I. (2016). GPS and in situ Swarm observations of the equatorial plasma density irregularities in the topside ionosphere. *Earth, Planets and Space*, *68*(1), 120. https://doi.org/10.1186/s40623-016-0490-5

Zhang, S., Nishimura, Y., Erickson, P. J., Aa, E., Kil, H., Deng, Y., Thomas, E. G., Rideout, W., Coster, A. J., Kerr, R., & Vierinen, J. (2022). Traveling Ionospheric Disturbances in the Vicinity of Storm-Enhanced Density at Midlatitudes. *Journal of Geophysical Research: Space Physics*, *127*(8). https://doi.org/10.1029/2022JA030429

Zhu, J., Ridley, A. J., & Deng, Y. (2016). Simulating electron and ion temperature in a global ionosphere thermosphere model: Validation and modeling an idealized substorm. *Journal of Atmospheric and Solar-Terrestrial Physics*, *138–139*, 243–260. https://doi.org/10.1016/j.jastp.2016.01.005

Zhu, Q., Deng, Y., Sheng, C., Anderson, P., & Bukowski, A. (2022). Impact of Soft Electron Precipitation on the Thermospheric Neutral Mass Density During Geomagnetic Storms: GITM Simulations. *Geophysical Research Letters*, *49*(11), e2021GL097260. https://doi.org/10.1029/2021GL097260